SCIENTIFIC REPORTS

Correspondence and
requests for materials
should be addressed to
Y.S. (hige@ncsimd.
kankyo.tohoku.ac.jp)

* These authors
contributed equally to
this work.

Long-term biopersistence of tangled oxidized carbon nanotubes inside and outside macrophages in rat subcutaneous tissue

Yoshinori Sato[1]*, Atsuro Yokoyama[2]*, Yoshinobu Nodasaka[2], Takao Kohgo[2], Kenichi Motomiya[1], Hiroaki Matsumoto[3], Eiko Nakazawa[3], Tomoko Numata[4], Minfang Zhang[5], Masako Yudasaka[5], Hideyuki Hara[6], Rikita Araki[6], Osamu Tsukamoto[7], Hiroaki Saito[8], Takeo Kamino[3], Fumio Watari[2] & Kazuyuki Tohji[1]

[1]Graduate School of Environmental Studies, Tohoku University, Sendai 980-8579, Japan, [2]Graduate School of Dental Medicine, Hokkaido University, Sapporo 060-8586, Japan, [3]Advanced Microscope Systems Design, Hitachi High-Technologies Corporations, Hitachinaka 312-0057, Japan, [4]Analytical Application Center, Horiba, Ltd., Tokyo 101-0031, Japan, [5]National Institute of Advanced Industrial Science and Technology, Tsukuba 305-8566, Japan, [6]Bruker BioSpin K. K., Yokohama 221-0022, Japan, [7]Netzsch Japan K. K., Yokohama 221-0022, Japan, [8]Graduate School of Engineering, Tohoku University, Sendai 980-8579, Japan.

Because of their mechanical strength, chemical stability, and low molecular weight, carbon nanotubes (CNTs) are attractive biological implant materials. Biomaterials are typically implanted into subcutaneous tissue or bone; however, the long-term biopersistence of CNTs in these tissues is unknown. Here, tangled oxidized multi-walled CNTs (t-ox-MWCNTs) were implanted into rat subcutaneous tissues and structural changes in the t-ox-MWCNTs located inside and outside of macrophages were studied for 2 years post-implantation. The majority of the large agglomerates were present in the intercellular space, maintained a layered structure, and did not undergo degradation. By contrast, small agglomerates were found inside macrophages, where they were gradually degraded in lysosomes. None of the rats displayed symptoms of cancer or severe inflammatory reactions such as necrosis. These results indicate that t-ox-MWCNTs have high biopersistence and do not evoke adverse events in rat subcutaneous tissue *in vivo*, demonstrating their potential utility as implantable biomaterials.

Because of their light weight and strong mechanical properties, graphite and C/C composites have been studied for their use as artificial bone and teeth since the 1980s[1]. Since the discovery of carbon nanomaterials (CNMs) such as fullerenes[2,3], carbon nanotubes (CNTs)[4–7], and carbon nanohorns[8], CNMs and their organic/inorganic hybrid materials have been considered for medical applications, for example, as carriers[9–11] for drug delivery systems, cell growth scaffolds[12–14], medical hyperthermia agents[15–17], fluorescence imaging agents[18,19], and ultrasound contrast agents[20]. For such applications, CNMs are injected or implanted into the body after being modified with functional groups or coated with a bioinert polymer, such as a polypeptide, polysaccharide, or polyethylene glycol. A fundamental knowledge of the biopersistence and metabolism of CNMs is vitally important for these applications[21]. For example, graphite has good biocompatibility[22] and its structure is not thought to be changed or biodegraded[1] within living organisms. However, the biological persistence of CNMs has not been clarified.

Recently, *in vitro* and *in vivo* studies have demonstrated the enzymatic oxidation of CNMs[23–29]. Carboxylated single-walled CNTs (COOH-SWCNTs) are catalytically biodegraded *in vitro* within several weeks by the plant-derived enzyme horseradish peroxidase in the presence of low concentrations of hydrogen peroxide (H_2O_2)[23]. These CNTs are also degraded by myeloperoxidase within neutrophils, both *in vitro* and *in vivo*[24,29]. Functional groups, such as the carboxylic groups of SWCNTs, increase the enzymatic oxidative degradation of CNTs[25,26]. Similarly, multi-walled CNTs (MWCNTs) are also partially biodegraded, but over a longer time period of several months[26,27]. Zhao and colleagues[27] suggested a layer-by-layer mechanism for the enzymatic oxidation of

COOH-MWCNTs, whereby the nanotube diameter is decreased while the length is maintained. The biodegradation rate of MWCNTs is increased by the introduction of nitrogen-containing functional groups[27,28]. For example, nitrogen-doped MWCNTs are completely enzymatically degraded within 80 days[27]. Amino-functionalized MWCNTs are partially degraded *in vivo* within the microglia of the brain cortex in 2 to 14 days[28]. These studies indicate that CNTs are rapidly engulfed and degraded by phagocytes, which is advantageous to their use as carriers for drug delivery systems.

Bulk biomaterials used as artificial organs or implantable cardiac pacemakers are not engulfed by phagocytes; these materials are present in the intercellular space and are covered with tissue for extended periods[30]. The potential applications of bulk CNT films[12–14,31–33] as scaffolds and of CNT blocks[34,35] or CNT composites[36–39] as artificial organs have been investigated previously. These studies suggested that the biodegradation of CNTs outside phagocytes and long-term biopersistence are crucial issues related to their use as bulk biomaterials; however, these issues require further investigation.

To fill the gap in the literature concerning the biopersistence of CNTs for implantation, we performed a long-term analysis of the biopersistence of tangled oxidized MWCNTs (t-ox-MWCNTs). In particular, we implanted t-ox-MWCNTs into the subcutaneous tissues of rats and investigated structural changes in the t-ox-MWCNTs located inside and outside of macrophages for up to 2 years after implantation using high-resolution transmission electron microscopy (HRTEM) and Raman scattering spectroscopy.

Results

Characteristics of t-ox-MWCNTs. The structure and surface state of t-ox-MWCNTs were clarified before the implantation in the rat (see Table 1). On average, the t-ox-MWCNTs contained 15 graphene layers and were 825 nm in length[40]. The mean inside and outside diameters were 8.1 nm and 17.8 nm, respectively, and a typical HRTEM image is shown in Fig. 1a. The MWCNTs displayed a tangled or curled morphology. The purity of the t-ox-MWCNTs was high, comprising 98.17 wt% C, 1.41 wt% Al, 0.26 wt% Fe, 0.01 wt% Mo, and 0.15 wt% Cr, as estimated using inductively coupled plasma-optical emission spectrometry (ICP-OES). HRTEM with energy-dispersive X-ray spectrometry revealed that the iron metals were covered with thick graphite layers, and aluminum was present as aluminum oxide.

The Fourier transform-infrared absorption (FT-IR) spectrum of t-ox-MWCNTs showed that the MWCNTs carried the following functional groups: aromatic C=C (1580 cm^{-1}), COOH (1198 cm^{-1}, stretching vibration of C-O; 1402 cm^{-1}, deformation vibration of O-H; 1720 cm^{-1}, stretching vibration of C=O), and O-H (3145 cm^{-1}, stretching vibration) (Fig. 1b). X-ray photoelectron spectroscopy and thermogravimetric analysis[26,41] showed that the t-ox-MWCNT surface was mainly modified with -OH and -COOH groups (Fig. S1), with quantities ranging from 4.2 to 4.8 mmol/g and 2.4 to 2.8 mmol/g, respectively (Fig. S2). Because the average specific surface area was 320 m^2/g, the number ratio of -OH groups, -COOH groups, and C atoms on t-ox-MWCNTs was 2 : 1 : 10. These oxygenated groups may have been negatively charged in water. The surface charge of the t-ox-MWCNTs was negative (-48.9 mV at pH 7.0), in contrast to the positive charge ($+44.5$ mV at pH 7.4) of asbestos (chrysotile A)[42]. Due to the many oxygenated groups, the solubility of t-ox-MWCNTs in distilled water (pH 6.8) and in phosphate-buffered saline (pH 7.0) was sufficiently high (0.10 and 0.01 mg/mL at room temperature, respectively)[40].

The Raman scattering spectrum of the t-ox-MWCNTs (Fig. 1c) showed the defect mode (D-band, 1350 cm^{-1}) and the transversal mode (G-band, 1590 cm^{-1}). Both bands were broad, and the D/G intensity ratio was 1.14 (SD $\pm$ 0.03). These spectral features suggested that the t-ox-MWCNTs were defective. This finding was consistent with the large number of surface functional groups. The electron spin resonance (ESR) signal of OH radicals generated from the Fenton reaction of H_2O_2[43] (see Methods) completely disappeared in the presence of t-ox-MWCNTs (Fig. 1d). This result indicated that the t-ox-MWCNTs scavenged the OH radicals.

Tissue response after implantation. We subcutaneously implanted t-ox-MWCNTs into male 6-week-old Wistar strain rats (weight: 160 $\pm$ 10 g). The Wistar strain rat is a standard species used for the biocompatibility testing of biomaterials[44] and was used to make histological observations of tissue responses to t-ox-MWCNTs. Two bilateral subcutaneous pockets were made in the thoracic region by incision under general anesthesia. A powdered form of t-ox-MWCNTs (<100 µg) was implanted in the pockets. The powdered form was chosen, expecting that the formation of large agglomerates prevented macrophages from engulfment of the t-ox-MWCNTs. At 1 week, 1 year, and 2 years after implantation (1 week, $n = 3$; 1 and 2 years, $n = 2$), segments of the subcutaneous tissue containing the t-ox-MWCNTs were excised and fixed. Two years was the longest possible follow-up period in this study because the average life expectancy of the male Wistar rat is 810 days. The specimens were fixed for histological observation with optical microscopy and HRTEM. The specimens for Raman scattering

Table 1	Characteristics of t-ox-MWCNTs	
Characteristic items	
Inside diameter (nm, mean $\pm$ SD)	8.1 $\pm$ 2.1
Outside diameter (nm, mean $\pm$ SD)	17.8 $\pm$ 6.4
Number of graphene layer (mean $\pm$ SD)	15.0 $\pm$ 5.0
Length (nm, mean $\pm$ SD)	825 $\pm$ 174
Structure	hollow and bamboo-like tubes
Morphology	curved and tangled
I_D/I_G value (mean $\pm$ SD)	1.14 $\pm$ 0.03
Surface modification	hydroxyl and carboxyl groups
OH coverage (mmol/g)	4.2–4.8
COOH coverage (mmol/g)	2.4–2.8
Specific surface area (m^2/g, mean $\pm$ SD)	320 $\pm$ 15
Zeta potential (mV, mean $\pm$ SD)	-48.9 ± 8.0
Solubility (mg/mL)*	0.10 (water) 0.01 (PBS)
Residue metals (wt%)	Al 1.41
	Fe 0.26
	Mo 0.01
	Cr 0.15

*Under room temperature, the pH values used for water and PBS were 6.8 and 7.0, respectively.
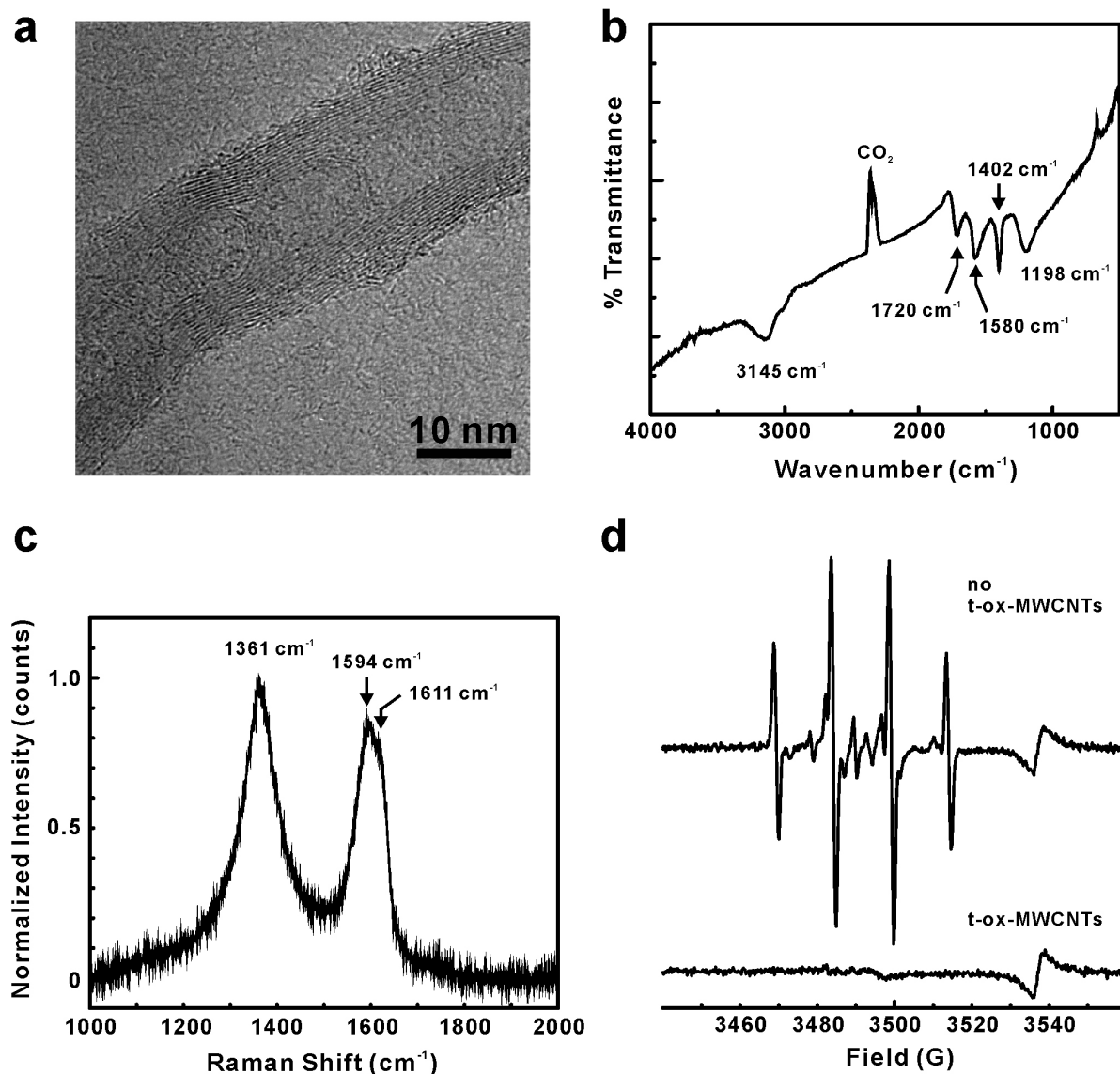
Figure 1 | Characterization of t-ox-MWCNTs used in this study. (a) HRTEM image, (b) FT-IR spectrum, and (c) Raman scattering spectrum of t-ox-MWCNTs. (d) ESR signals observed in the absence (top) and presence (bottom) of t-ox-MWCNTs. The signal intensity is proportional to the amount of the ·OH free radical generated by the Fenton reaction in solution. No signal was observed in the presence of t-ox-MWCNTs, which suggests that t-ox-MWCNTs possess scavenging activity. The HRTEM image is representative of greater than 100 independent observation areas. The FT-IR, Raman scattering, and ESR spectra are representative of three, ten, and two independent experiments, respectively.

spectroscopy measurements were not fixed so that Raman peaks with good signal-to-noise ratios could be detected.

Tissue response at 1 week. During the wound healing process, granulation tissues replace the fibrin clot in the healing wound and fill the wound. Fibroblasts appear and produce extracellular matrix and collagen for wound healing. At 1 week after the subcutaneous implantation of the t-ox-MWCNTs in rats, t-ox-MWCNT agglomerates were found in the granulation tissue (Fig. 2a). Close observation of the granulation tissues revealed that most of the large t-ox-MWCNT agglomerates (size > approximately 5 μm) were found among the fibroblasts and foreign body giant cells (Fig. 2b); the latter are a collection of fused macrophages generated in response to large foreign bodies. The small t-ox-MWCNTs aggregates (size < 5 μm) were internalized by the macrophages (Fig. 2b).

Observation by HRTEM revealed that the large t-ox-MWCNT agglomerates were hemmed in by many macrophages (Fig. 2c).

The small t-ox-MWCNT agglomerates were found in the cytoplasm of macrophages, where secondary lysosomes, vesicles, and mitochondria were also observed (Fig. 2d and e). Some of the small t-ox-MWCNTs agglomerates were found in secondary lysosomes (Fig. 2d) and endosomes (the arrows in Fig. 2e indicate the endosome membrane structure). In addition, a few macrophages did not have well-developed organelles (Fig. 2f). Furthermore, phagocytes were unable to engulf the large t-ox-MWCNT aggregates. These results suggest that the phagocytes did not react strongly to the aggregates, unlike frustrated phagocytes, which are capable of engulfing long asbestos fibers[45,46].

Tissue response at 1 year. At 1 year after implantation, large agglomerates of t-ox-MWCNTs were found within the thin connective tissue, which comprised adipose tissue (Fig. S3a); these agglomerates were surrounded by foreign body giant cells that were most likely foreign body granulomas (Fig. S3b). HRTEM revealed small t-ox-MWCNT agglomerates within macrophages (Fig. S3b),
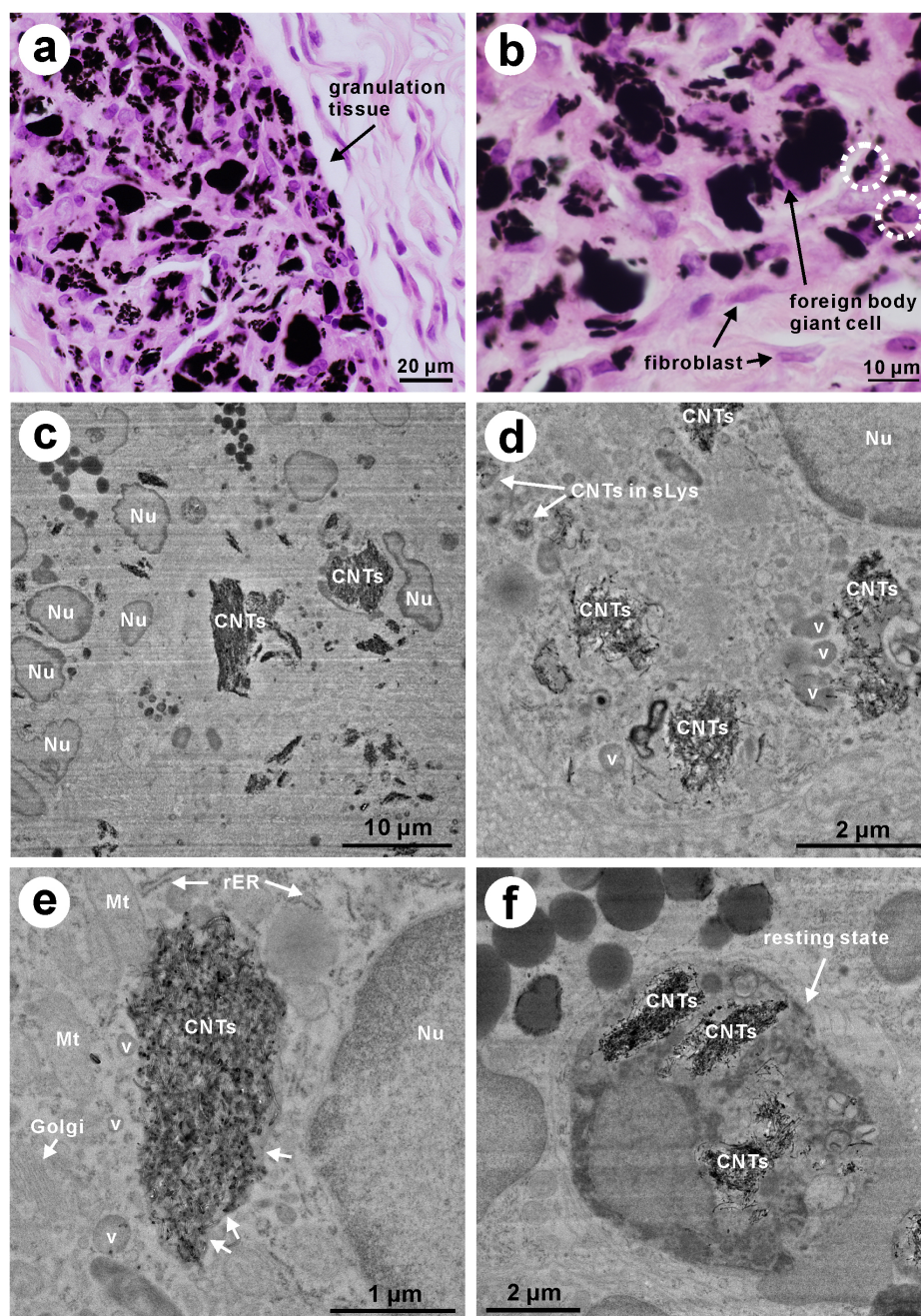
Figure 2 | Histological and HRTEM images of t-ox-MWCNTs in the tissue at 1 week after implantation. (a) Optical micrograph. (b) High-magnification optical micrograph. Large and small t-ox-MWCNT agglomerates appeared as black spots surrounded by granulation tissue with macrophages (dotted circles), foreign body giant cells, and fibroblasts. (c to f) HRTEM images. Large t-ox-MWCNT agglomerates were hemmed in by many macrophages (Fig. 2c). Most of the small t-ox-MWCNT agglomerates existed in the cytoplasm of macrophages, where secondary lysosomes (sLys), vesicles (v), and mitochondria (Mt) were observed (Fig. 2d and e). White arrows in Fig. 2e point to an endosome membrane. Macrophages engulfing t-ox-MWCNTs appeared to be in a resting state (Fig. 2f). Nu, nucleus; rER, rough endoplasmic reticulum; Golgi, Golgi body. The histological and HRTEM images are representative of greater than 100 independent observations areas in each implanted t-ox-MWCNT.

specifically in the lysosomes (Fig. S3c). Some of the small agglomerates were separated into even smaller agglomerates (Fig. S3c).

Tissue response at 2 years. The tissue response at 2 years after implantation was almost the same as that at 1 year after implantation. Macrophages, fibroblasts, multinucleated foreign body giant cells, and capillaries were observed in the granulation tissue (Fig. 3a and b). As the cytoplasmic processes of the macrophage invaginated (see the invaginating cytoplasmic process

in Fig. 3c)[47], many mitochondria and primary lysosomes (white arrows in Fig. 3c) were observed within the macrophage. These observations implied that the t-ox-MWCNTs underwent activated macrophage-mediated clearance (Fig. 3a and Fig. S4).

Poland and colleagues reported the effect of the length of MWCNTs on the inflammatory response after introduction of the MWCNTs into the abdominal cavity of mice for 7 days[48], and Nagai and colleagues investigated the influence of the diameter of the MWCNTs on the inflammatory response after intraperitoneal injection of the MWCNTs into rats for 1 month[49]. Both studies showed
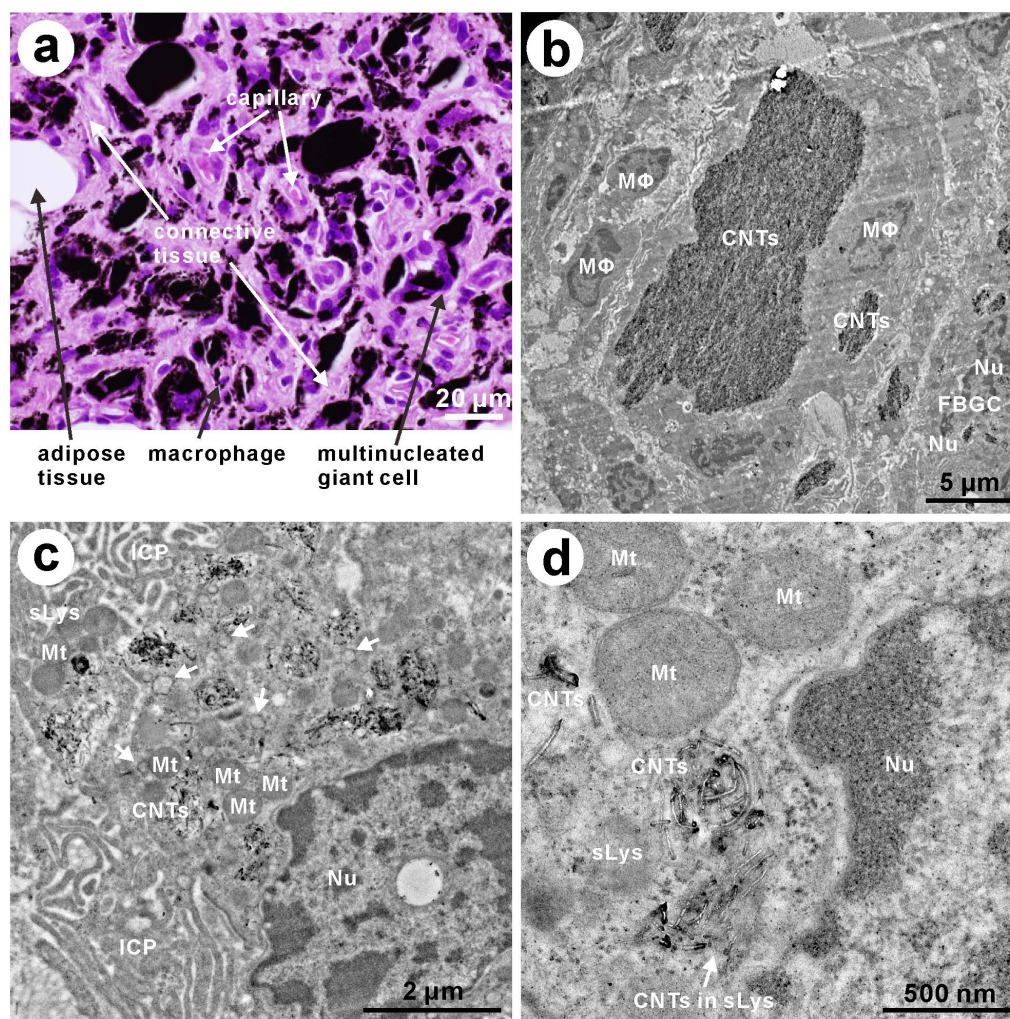
Figure 3 | Histological and HRTEM images of t-ox-MWCNTs in the tissue at 2 years after implantation. (a) Optical micrograph and (b to d) HRTEM images. Macrophages (MΦ), fibroblasts, multinucleated foreign body giant cells (FBGC), and capillaries were observed in the granulation tissue. The thin fibrous connective tissue was well organized (Fig. 3a and b). Many mitochondria and primary lysosomes (white arrows in Fig. 3c) were observed in the macrophage as the cytoplasmic process of the macrophage invaginated. ICP, invaginating cytoplasmic process. The histological and HRTEM images are representative of greater than 100 independent observations areas in each implanted t-ox-MWCNT.

that thin, tangled MWCNTs did not induce severe inflammation. Nagai and colleagues also tested the carcinogenicity of tangled MWCNTs after their intraperitoneal injection into rats, which allowed the MWCNTs to directly interact with mesothelial cells immediately after administration[49]. Their data showed that the tangled CNTs were less toxic and less carcinogenic. The high biocompatibility of functionalized SWCNTs[24,50,51] and MWCNTs[20,40,50–54] in various tissues and cells has been well characterized. The data presented here suggest that the t-ox-MWCNTs used in this study are also biocompatible materials. All of the rats included in the study survived, and symptoms of cancer or severe inflammatory changes such as necrosis were not observed in the subcutaneous tissue for up to 2 years after implantation. These findings suggested that the toxicity of the t-ox-MWCNTs was not severe.

Structural characterization of the implanted t-ox-MWCNTs. Figures 4a and b show the typical Raman spectra of the large t-ox-MWCNT agglomerates at 1 week (blue line) and 2 years (red line) in the intercellular space and in macrophages, respectively. The spectra were measured in the areas of the white circles in the inset images in Fig. 4. The average D/G intensity ratio of t-ox-MWCNTs in the intercellular space after 1 week was 1.15 (SD ± 0.06); after 2 years

it was 1.14 (SD ± 0.06). These values were similar to the original value of 1.14 (SD ± 0.03). This similarity indicated that the structural defects of the large t-ox-MWCNT agglomerates in the intercellular space did not increase.

By contrast, the typical Raman spectra of the small t-ox-MWCNT agglomerates in the macrophages at 1 week were different from those at 2 years (Fig. 4b). The average D/G intensity ratio of t-ox-MWCNTs in the macrophages was 1.14 (SD ± 0.04) at 1 week, which increased to 1.23 (SD ± 0.03) at 2 years. Similar spectral changes are observed when ox-SWCNTs[23–26] or ox-MWCNTs[26] are enzymatically destroyed. Apparently, these defects/deformations occurred during the 2 years of localization within macrophages.

We further studied the structure of the t-ox-MWCNTs by HRTEM. At 1 week after implantation, we clearly observed the (002) lattice image of t-ox-MWCNTs in the intercellular space (Fig. 5a and Fig. S5). The t-ox-MWCNT agglomerates in endosomes (Fig. 5b) also displayed (002) lattice images (Fig. 5c and 5d, and Fig. S6). The typical electron diffraction patterns of the aggregated t-ox-MWCNTs inside (in secondary lysosomes) (Fig. 5e and Fig. S7) and outside (Fig. 5f and Fig. S8) of the macrophages at 1 week after implantation were assigned to the (002) Debye ring. These patterns were assigned to the ring rather than to the spots because the
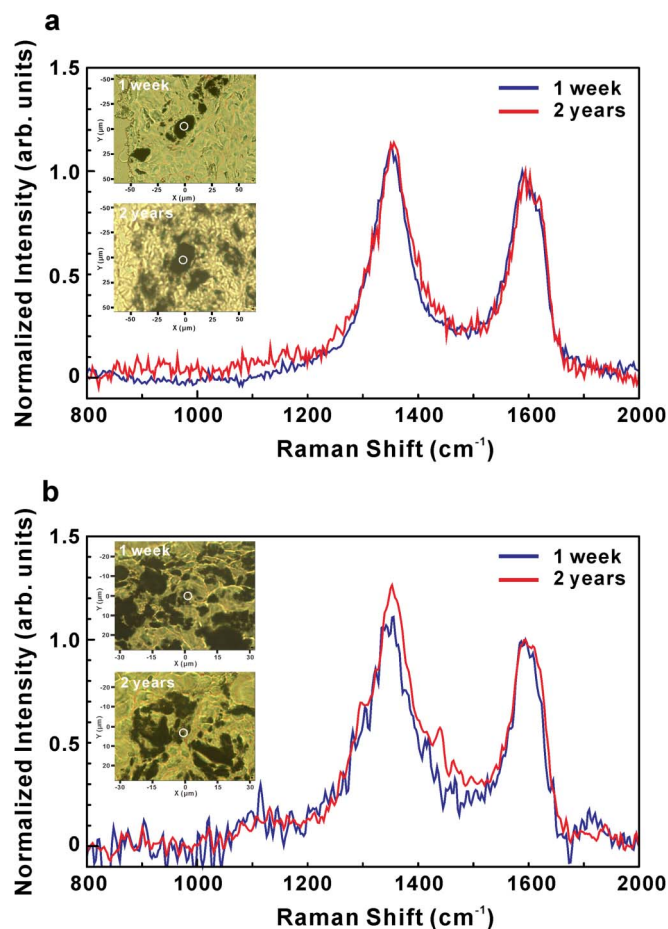
Figure 4 | Raman scattering spectra of t-ox-MWCNTs in the tissue over time. Typical Raman scattering spectra of t-ox-MWCNTs in (a) the intercellular space and (b) macrophages at 1 week and 2 years after implantation. Each inset shows an optical micrograph of the specimen being measured, and the white circle indicates the measured area. The Raman scattering spectra are representative of ten independent observations areas in each implanted t-ox-MWCNT.

Figure 5 | HRTEM images and electron diffractions of t-ox-MWCNTs in the tissue at 1 week after implantation. (a) HRTEM image of t-ox-MWCNTs in the intercellular space at 1 week after implantation. The black shaded area is an iron particle, which is an impurity in the t-ox-MWCNTs. (b) HRTEM image of t-ox-MWCNT agglomerates in an endosome, as shown in Fig. 2e. (c, d) High-magnification HRTEM images of t-ox-MWCNTs in an endosome. (e, f) Typical electron diffraction patterns (inset) taken from aggregated t-ox-MWCNTs (white dashed circle) inside (in secondary lysosome) (Fig. 5e) and outside (Fig. 5f) a macrophage at 1 week after implantation. The insets in panels (a), (c), and (d) are high-magnification images of the boxed areas indicated. The scale bar in all insets is 5 nm. The HRTEM images are representative of greater than 100 independent observation areas in each implanted t-ox-MWCNT.

t-ox-MWCNT tubular axes showed a random orientation. The means and standard deviations of the (002) spacing inside and outside the macrophages were 3.482 ± 0.0089 Å and 3.481 ± 0.0153 Å, respectively. These measurements coincided with those of the t-ox-MWCNTs before implantation (3.488 ± 0.0091 Å). The Debye ring was not detected in the tissue prior to t-ox-MWCNT implantation.

At 2 years after implantation, the (002) lattice image of the t-ox-MWCNTs was clearly observed in the intercellular space (Fig. 6a and Fig. S9) and in the macrophage (Fig. 6b and 6c, and Fig. S10). The 3–5 nm thick layers on the surface of the t-ox-MWCNTs (white arrows in Fig. 6d and Fig. S11) were assumed to be protein layers because similar protein layers are formed on CNTs[55]. Because the t-ox-MWCNTs were not covered with these layers at 1 week after implantation, the proteins may have been deposited on the t-ox-MWCNTs over the 2 years. The careful observation of the t-ox-MWCNTs within secondary lysosomes in the macrophage (Fig. 6e, and Fig. S12 and S13) showed that the outer layers of the t-ox-MWCNTs did not display clear lattice images and had a more turbostratic structure[56,57] (see white arrows in Fig. 6f) than those observed after 1 week (Fig. 5c and 5d) or 1 year[58].

The typical electron diffraction patterns (insets of Fig. 7b and 7d) of the aggregated t-ox-MWCNTs located inside (in secondary lysosomes) (Figs. 7a–b and Fig. S14) and outside (Figs. 7c–d and Fig. S15)
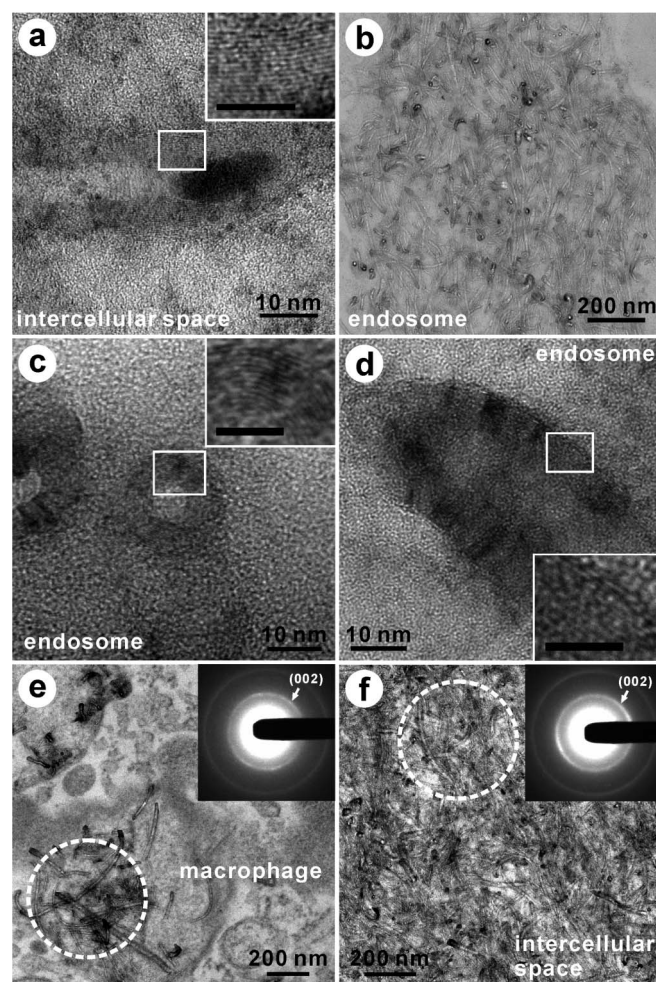
of the macrophage at 2 years post-implantation had (002) spacing of 3.482 ± 0.0155 and 3.483 ± 0.0085 Å, respectively, which coincided with the (002) spacing of t-ox-MWCNTs implanted for 1 week. This result was reasonable because the layers of the t-ox-MWCNTs inside and outside of macrophages at 1 week and 2 years appeared similar (Figs. 5–6). In secondary lysosomes (Figs. 7e–f and Fig. S16) at 2 years, however, the aggregated t-ox-MWCNTs had the (002) spacing of 3.530 ± 0.0211 Å (insets of Fig. 7f and Fig. S16), which was slightly larger (by approximately 1.2%) than that of the t-ox-MWCNTs at 1 week post-implantation. This difference could be due to the turbostratic structure of the outer layer of the t-ox-MWCNTs existing in the lysosomes (Fig. 6f). On the basis of these findings, we concluded that the t-ox-MWCNTs were not degraded outside the macrophages, but that the outer graphene layers of some t-ox-MWCNTs were degraded inside macrophages.
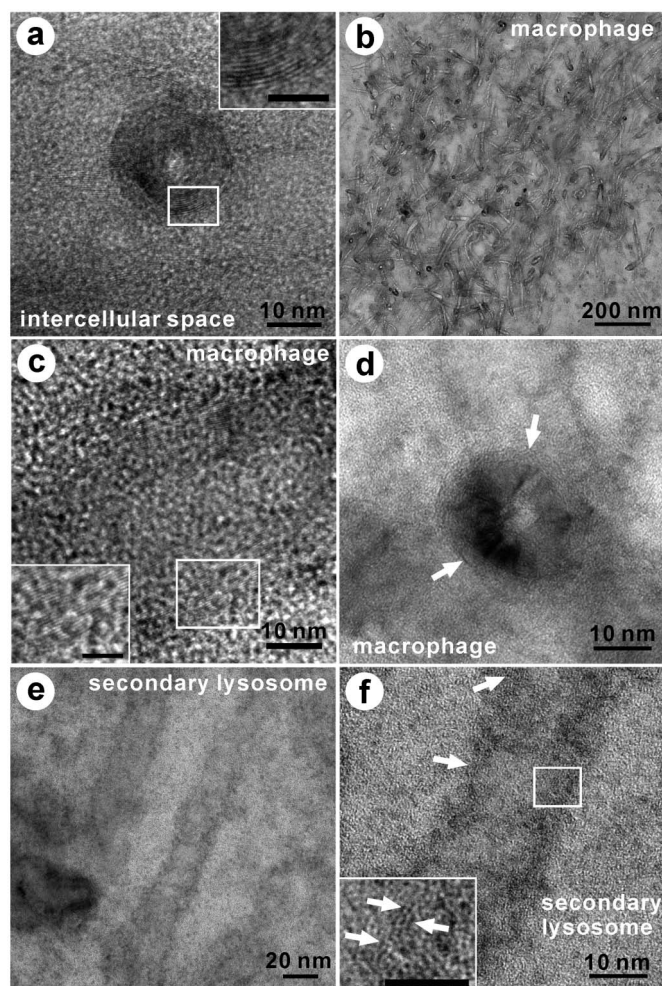
Figure 6 | HRTEM images of t-ox-MWCNTs in the tissue at 2 years after implantation. (a) HRTEM image of t-ox-MWCNTs in the intercellular space. (b) Low-magnification HRTEM image of t-ox-MWCNTs in the macrophage. (c) High-magnification HRTEM image of t-ox-MWCNTs in the macrophage. (d) HRTEM image of a 3–5 nm thick layer (white arrows) on the surface of a t-ox-MWCNT. (e) HRTEM image of t-ox-MWCNTs in a secondary lysosome in a macrophage. (f) High-magnification HRTEM image of the image shown in panel (e). The lattice images of the outer layers of MWCNTs are not clearly defined (white arrows). The insets in panels (a), (c), and (f) are high-magnification images of the boxed areas indicated. The scale bar in all insets is 5 nm. The HRTEM images are representative of greater than 100 independent observation areas in each implanted t-ox-MWCNT.

Figure 7 | Electron diffractions of t-ox-MWCNTs in the tissue at 2 years after implantation. (a) HRTEM image of t-ox-MWCNTs in the secondary lysosome inside a macrophage. (b) High-magnification HRTEM image of the boxed area shown in panel (a) and the electron diffraction pattern (inset) of the aggregated t-ox-MWCNTs (indicated by a white dashed circle). (c) HRTEM image of t-ox-MWCNTs in the intercellular space. (d) High-magnification TEM image of the boxed area shown in panel (c) and the electron diffraction pattern (inset) of aggregated t-ox-MWCNTs. (e) HRTEM image of t-ox-MWCNTs in the secondary lysosome inside a second macrophage. (f) High-magnification TEM image of the boxed area in panel (e) and the electron diffraction pattern (inset) of aggregated t-ox-MWCNTs. Nu, nucleus. The HRTEM images are representative of greater than 100 independent observation areas in each implanted t-ox-MWCNT.

Discussion

Soon after the t-ox-MWCNTs were implanted, their small-sized agglomerates were engulfed by macrophages and internalized in lysosomes. Over the 2 years, the t-ox-MWCNT-containing macrophages survived for a half year or less and died, then the residues were taken up by another macrophages. Repeating the cycles for two years, however, t-ox-MWNTs were not much damaged in our study. The slight damages of t-ox-MWNTs were found on their outside layers which were, probably, enzymatically oxidized in the lysosomes, as previously reported[23–27].

Meanwhile, the large t-ox-MWCNT agglomerates in the intercellular space were hemmed in by macrophages and foreign body giant cells, but no severe inflammatory response was observed in the tissues. Frustrated phagocytes that have engulfed long asbestos fibers release large amounts of reactive oxygen species, inflammatory mediators, a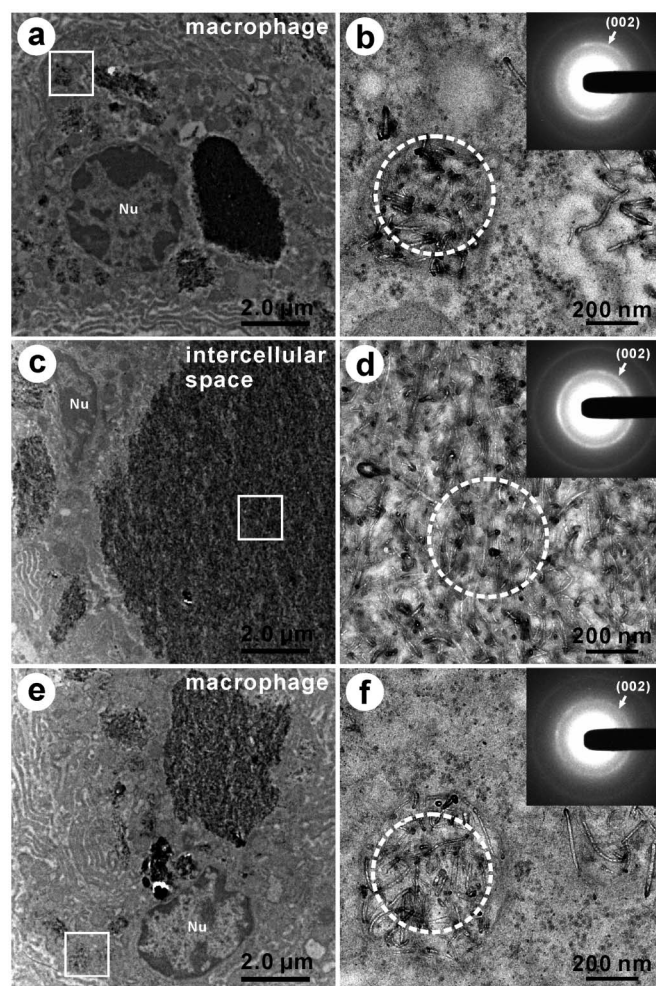nd growth factors, and cause severe inflammation[45,46]. However, a strong inflammatory reaction was not detected even in the early stage after implantation of t-ox-MWCNTs; after 2 years, the t-ox-MWCNTs were covered with thin fibrous connective tissue that reacts with bio-inert materials[44]. In this study, we evaluated the biocompatibility of t-ox-MWCNTs histologically, not biochemically. In the future, the immunological responses to t-ox-MWCNTs should be clarified by performing long-term biochemical investigations.

In conclusion, using HRTEM and Raman scattering spectroscopy, we characterized the structure of t-ox-MWCNTs that were implanted for 2 years in the subcutaneous tissue of rats. Large t-ox-MWCNT agglomerates were observed in the intercellular space and were not engulfed by macrophages, whereas small t-ox-MWCNT agglomerates were engulfed by macrophages. The outer layers of ox-MWCNTs in the lysosomes of macrophages were biodegraded, although not completely (Fig. 8a). The large
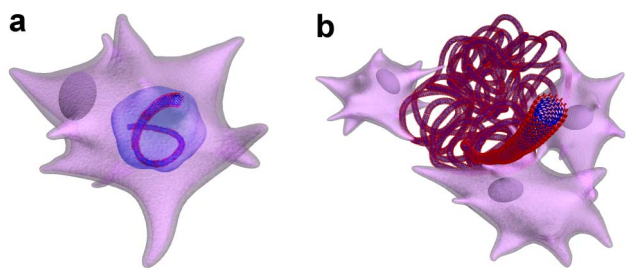
Figure 8 | Illustration of t-ox-MWCNTs in rat subcutaneous tissue at 2 years after implantation. (a) Illustration of t-ox-MWCNTs in the secondary lysosome within a macrophage. The outer layers of t-ox-MWCNTs in the lysosomes of macrophages are partially biodegraded. (b) Illustration of t-ox-MWCNTs located outside the macrophage. The large t-ox-MWCNT agglomerates present in the intercellular space are not biodegraded.

t-ox-MWCNT agglomerates in the intercellular space were not bio-degraded at 2 years after implantation (Fig. 8b). Indeed, at 2 years, granulomatous inflammation was observed around the large t-ox-MWCNT agglomerates, and thin fibrous connective tissue had formed. Moreover, even the early stages of severe inflammatory changes, such as necrosis and carcinogenesis, were not observed in the tissues. These findings implied that the toxicity of the t-ox-MWCNTs was not severe. In agreement with the relatively low tox-icity of the t-ox-MWCNTs used here, a previous study reported that MWCNTs implanted into subcutaneous tissue on the backs of gen-etically-modified rasH2 mice were less carcinogenic than carbon black derived from tattoo ink[59].

For use as artificial bone, prosthetic joints, and dental implants, biomaterials must be strong, biocompatible, and biopersistent. As implant materials, CNTs bearing -OH and -COOH functional groups must be biocompatible and show good biopersistence. The results presented here demonstrate that CNT composites are durable and are therefore resistant to attack by macrophages. We believe our finding that t-ox-MWCNTs show long-term biopersistence *in vivo*, both inside and outside macrophages, will serve as a guideline for designing CNM- or CNT-including biomaterials for medical implant applications.

Methods

Preparation of t-ox-MWCNTs. *Purification.* MWCNTs (diameter: 20–40 nm; length: 5–20 μm) from NanoLab, Inc., synthesized by the chemical vapor deposition (CVD) method, were used in this study. The purity was about 80 wt%, with impurities such as amorphous carbon, Al (5.73 wt%), Fe (4.43 wt%), Mo (1.27 wt%), and Cr (0.07 wt%), as determined by ICP-OES (Thermo Elemental Co. Ltd., USA). As-grown soot (100 mg) was burnt in air at 500°C for 90 minutes. The burnt soot (26.8 wt% loss) was introduced into a flask containing 6 mol/L HCl to dissolve the Fe, Mo, and Cr. The acid solution was filtered through a membrane filter. The filtered cake was transferred to a flask containing 1.0 L of NaOH (2 mol/L) and refluxed at 100°C for 15 hours to dissolve the aluminum oxides. The resultant suspension was filtered through a membrane filter, and the filtered cake was washed with hot water. Finally, the samples were dried *in vacuo* at 100°C for 24 hours.

Cutting. Purified MWCNTs (100 mg) were suspended in a 100 mL flask containing a $3:1$ (v/v%) mixture of concentrated 95% H_2SO_4:60% HNO_3 and exposed to ultra-sonic irradiation (200 W, 39 kHz; UT-204, SHARP, Japan) at 40°C for 5 hours. The acid-treated MWCNTs were filtered with a membrane filter, and the filtered cake was washed with water. Finally, samples were dried *in vacuo* at 100°C for 24 hours.

Separation. Cut MWCNTs (20 mg) were suspended in a flask containing 400 mL of ethanol and subjected to ultrasonic irradiation for 1 hour. The MWCNT aggregate was filtered through a 37 μm aperture screen to separate out the few-microns-long MWCNTs. The cut MWCNTs in the supernatant were size-separated by a multistep microfiltration process that used a series of polycarbonate membrane filters with cylindrical pore diameters of 2.0, 1.2, 0.8, and 0.4 μm. Each filtered cake sample was dried *in vacuo* at 100°C for 24 hours. We used the filtered cake sample on 2.0 μm pore size membrane filter as a testing sample.

Characterization of t-ox-MWCNTs. *SEM, HRTEM, and STEM analyses.* The morphology and structure of the t-ox-MWCNTs were determined by SEM (S-4100, Hitachi, Japan), HRTEM (HF-2000, Hitachi, Japan), and STEM (HD-2700, Hitachi, Japan) using a field emission gun. The SEM, HRTEM, and STEM instruments were operated at 5, 200, and 200 kV, respectively. The mean diameter and length of the t-ox-MWCNTs were determined from n = 100 independent observations.

XPS analysis. The detailed elemental carbon compositions of ox-MWCNTs were characterized by X-ray photoelectron spectroscopy equipped with an Al anode (Al Kα). Metal impurities were detected by ICP-OES.

Specific surface area analysis. The specific Brunauer-Emmett-Teller surface area was measured on an NOVA 1200 porosimeter (Quantachrome Instruments, USA) by nitrogen adsorption at −196°C. The mean value was determined from n = 3 inde-pendent experiments.

Thermogravimetric analysis. Before each measurement, the samples were degassed at 150°C for 24 hours under vacuum (<1.0 Pa). The weight loss of t-ox-MWCNTs and the decomposed gas from t-ox-MWCNTs were measured from 25 to 1000°C under an argon gas flow by high-resolution thermogravimetric analysis equipped with a mass spectrometer (STA 449 F1 Jupiter, NETZSCH, Germany).

Infrared spectroscopy analysis. The vibrational modes of the modified nanotube sam-ples were characterized by FT-IR (Avatar 380, Thermo Electron Co. Ltd., USA). The samples were measured inside a KBr pellet.

Raman scattering spectroscopy analysis. Raman scattering spectroscopy studies were performed to analyze the vibrational modes of the graphitic materials. XploRA and LabRAM HR evolution microscopes (Horiba Corp., Japan) were used. These mea-surements were performed at room temperature (25°C) using an Excimer laser (532 nm). To detect the spectrum of t-ox-MWCNTs in the tissue, the sample was irradiated with a laser power of 0.1 mW (after confirming that this laser power would not damage the t-ox-MWCNTs). Figure S17 shows a typical optical micrograph of t-ox-MWCNTs in the tissue at 1 week after implantation (Fig. S17a) and the corres-ponding Raman mapping image (Fig. S17b) and Raman spectra (Fig. S17c). The Raman spectrum from the dark red area of the Raman image displays the D-band (1350 cm^{-1}) and G-band (1590 cm^{-1}) related to carbon materials (top in Fig. S17c). The D- and G-bands were not detected in the Raman spectrum from the green area of the Raman image (bottom in Fig. S17c). Thus, the red and green areas corresponded to the t-ox-MWCNTs and to the cells in the tissue, respectively. Areas were selected for targeting and measuring the Raman spectrum of the specimen. Ten Raman spectra in each implanted t-ox-MWCNT were measured.

Zeta potential analysis. The surface charges of the modified nanotube samples were characterized by measuring the zeta potential (ZEECOM ZC2000, Microtec, Japan). The sample was dispersed in distilled water (pH 7.0), and the dispersions were measured at room temperature (27°C). The mean value was determined from n = 3 independent experiments.

Solubility analysis. The solubilities of the t-ox-MWCNTs were determined by mea-suring the dispersed concentration as a function of the sedimentation time at room temperature. The dispersed concentration was measured by ultraviolet-visible absorption spectroscopy (U-3300, Hitachi, Japan). The initial concentration of all MWCNT samples was 0.1 mg/mL. The solubility of the t-ox-MWCNTs was defined as the concentration that was stable at 500 hours. The solvents were distilled water and a phosphate-buffered saline without calcium or magnesium ions.

Radical scavenging analysis. The scavenging potency of t-ox-MWCNTs to OH radi-cals was measured as previously described[28]. The generation of radical species was monitored by ESR spectroscopy (E580, Bruker BioSpin, Germany) using the spin-trapping technique with 5,5-dimethyl-1-pyrroline-*N*-oxide (DMPO) as the trapping agent. The OH radicals were generated by adding 250 μL of a 0.2 mol/L solution of H_2O_2 in water to a solution containing 0.025 mol/L DMPO and 1.7 mmol/L FeSO$_4$ in 0.17 mol/L potassium phosphate buffer, pH 7.4. The Fenton reaction, which gener-ates OH radicals, is as follows: $Fe^{2+} + H_2O_2 \rightarrow Fe^{3+} + \cdot OH + OH^-$. After OH radicals were generated, the intensity of the ESR spectrum of the DMPO/OH adduct was measured. The ESR spectra of the t-ox-MWCNTs were determined based on measurements obtained from two investigations.

Histological observation and characterization of t-ox-MWCNTs in the tissue.
TEM analysis. The fixed specimens were divided into two parts. One part was examined by optical microscopy. These specimens were embedded in paraffin, stained with hematoxylin and eosin, and observed by optical microscopy. The other part was observed by TEM. These specimens were post-fixed with 1% OsO$_4$ and routinely embedded in epoxy resin after dehydration. Ultrathin sections (approximately 80 nm thick) were cut with a diamond knife and stained with uranyl acetate and lead citrate. Stained sections were placed on a supporting carbon mesh grid and observed by TEM at voltages of 75 kV (H-800, Hitachi, Japan), 120 kV (H-7650, Hitachi, Japan), and 300 kV (H-9500, Hitachi, Japan). Electron diffraction patterns of the ox-MWCNTs were observed by HRTEM at voltages of 200 kV (HF-2000 and HF-3300, Hitachi, Japan). For each sample (prior to implantation, 1 week

after implantation, and 2 years after implantation), 11–35 electron diffraction patterns were measured. Each electron diffraction pattern displayed information derived from agglomerates consisting of a few tens of MWCNTs. The average (002) spacing of each sample was determined as the distance between the incident electron beam point and the brightest diffraction point.

1. Bokros, J. C. Carbon Biomedical Devices. *Carbon* **15**, 355–371 (1977).
2. Kroto, H. W., Heath, J. R., Obrien, S. C., Curl, R. F. & Smalley, R. E. C$_{60}$ - Buckminsterfullerene. *Nature* **318**, 162–163 (1985).
3. Krätschmer, W., Lamb, L. D., Fostiropoulos, K. & Huffman, D. R. Solid C60: a new form of carbon. *Nature* **347**, 354–358 (1990).
4. Oberlin, A., Endo, M. & Koyama, T. Filamentous growth of carbon through benzene decomposition. *J. Cryst. Growth* **32**, 335–349 (1976).
5. Iijima, S. Helical microtubules of graphitic carbon. *Nature* **354**, 56–57 (1991).
6. Iijima, S. & Ichihashi, T. Single-shell carbon nanotubes of 1-nm diameter. *Nature* **363**, 603–605 (1993).
7. Bethune, D. S. et al. Cobalt-catalysed growth of carbon nanotubes with single-atomic-layer walls. *Nature* **363**, 605–607 (1993).
8. Iijima, S. et al. Takahashi, K. Nano-aggregates of single-walled graphitic carbon nano-horns. *Chem. Phys. Lett.* **309**, 165–170 (1999).
9. Kostarelos, K., Bianco, A. & Prato, M. Promises, facts and challenges for carbon nanotubes in imaging and therapeutics. *Nat. Nanotech.* **4**, 627–633 (2009).
10. Nard-Moyon, C. M., Kostarelos, K., Prato, M. & Bianco, A. Functionalized carbon nanotubes for probing and modulating molecular functions. *Chem. Biol.* **17**, 107–115 (2010).
11. Fabbro, C. et al. Targeting carbon nanotubes against cancer. *Chem. Comm.* **48**, 3911–3926 (2012).
12. Mattson, M. P., Haddon, R. C. & Rao, A. M. Molecular functionalization of carbon nanotubes and use as substrates for neuronal growth. *J. Mol. Neurosci.* **14**, 175–182 (2000).
13. Aoki, N. et al. Cell Culture on a Carbon Nanotube Scaffold. *J. Biomed. Nanotechnol.* **1**, 402–405 (2005).
14. Usui, Y. et al. Carbon nanotubes with high bone-tissue compatibility and bone-formation acceleration effects. *Small* **4**, 240–246 (2008).
15. Zhang, M. et al. Fabrication of ZnPc/protein nanohorns for double photodynamic and hyperthermic cancer phototherapy. *Proc. Natl. Acad. Sci. U. S. A.* **105**, 14773–14778 (2008).
16. Miyako, E. et al. A photo-thermal-electrical converter based on carbon nanotubes for bioelectronic applications. *Angew. Chem. Int. Ed.* **50**, 1–6 (2011).
17. Miyako, E. et al. Photothermic regulation of gene expression triggered by laser-induced carbon nanohorns. *Proc. Natl. Acad. Sci. U. S. A.* **109**, 7523–7528 (2012).
18. Cherukuri, P., Bachilo, S. M., Litovsky, S. H. & Weisman, R. B. Near-infrared fluorescence microscopy of single-walled carbon nanotubes in phagocytic cells. *J. Am. Chem. Soc.* **126**, 15638–15639 (2004).
19. Welsher, K., Liu, Z., Daranciang, D. & Dai, H. Selective probing and imaging of cells with single walled carbon nanotubes as near-infrared fluorescent molecules. *Nano Lett.* **8**, 586–590 (2008).
20. Delogu, L. G. et al. Functionalized multiwalled carbon nanotubes as ultrasound contrast agents. *Proc. Natl. Acad. Sci. U. S. A.* **109**, 16612–16617 (2012).
21. Kane, A. B. & Hurt, R. H. Nanotoxicology: The asbestos analogy revisited. *Nat. Nanotech.* **3**, 378–389 (2008).
22. Gott, V. L., Whiffen, J. D. & Dutton, R. C. Heparin bonding on colloidal graphite surfaces. *Science* **142**, 1297–1298 (1963).
23. Allen, B. et al. Mechanistic Investigations of Horseradish Peroxidase-Catalyzed Degradation of Single-Walled Carbon Nanotubes. *J. Am. Chem. Soc.* **131**, 17194–17205 (2009).
24. Kagan, V. E. et al. Carbon nanotubes degraded by neutrophil myeloperoxidase induce less pulmonary inflammation. *Nat. Nanotech.* **5**, 354–359 (2010).
25. Liu, X. Y., Hurt, R. H. & Kane, A. B. Biodurability of single-walled carbon nanotubes depends on surface functionalization. *Carbon* **48**, 1961–1969 (2010).
26. Russier, J. et al. Oxidative biodegradation of single- and multi-walled carbon nanotubes. *Nanoscale* **3**, 893–896 (2011).
27. Zhao, Y., Allen, B. L. & Star, A. Enzymatic degradation of multiwalled carbon nanotubes. *J. Phys. Chem. A* **115**, 9536–9544 (2011).
28. Nunes, A. et al. In vivo degradation of functionalized carbon nanotubes after stereotactic administration in the brain cortex. *Nanomedicine (Lond)* **7**, 1485–1494 (2012).
29. Shvedova, A. A. et al. Impaired clearance and enhanced pulmonary inflammatory/fibrotic response to carbon nanotubes in myeloperoxidase-deficient mice. *PLoS One* **7**, e30923 (2012).
30. Hench, J. W. *Biomaterials, Artificial Organs and Tissue Engineering*, eds by Hench, L. L. & Jones, J. R., pp55–73 (Woodhead Publishing Limited, Cambridge, 2005).
31. Lovat, V. et al. Carbon nanotube substrates boost neuronal electrical signaling. *Nano Lett.* **5**, 1107–1110 (2005).
32. Zanello, L. P., Zhao, B., Hu, H. & Haddon, R. C. Bone cell proliferation on carbon nanotubes. *Nano Lett.* **6**, 562–567 (2006).
33. Boccaccini, A. R. et al. Carbon nanotube coatings on Bioglass-based tissue engineering scaffolds. *Adv. Func. Mater.* **17**, 2815–2822 (2007).
34. Sato, Y. et al. In vivo rat subcutaneous tissue response of binder-free multi-walled carbon nanotube blocks cross-linked by de-fluorination. *Carbon* **46**, 1927–1934 (2008).
35. Wang, W. et al. Preparation and characteristics of a binderless carbon nanotube monolith and its biocompatibility. *Mater. Sci. Eng. C* **28**, 1082–1086 (2008).
36. Tran, P. A., Zhang, L. & Webster, T. J. Carbon nanofibers and carbon nanotubes in regenerative medicine. *Adv. Drug. Deliv. Rev.* **61**, 1097–1114 (2009).
37. Kalmodia, S. et al. Microstructure, mechanical properties, and in vitro biocompatibility of spark plasma sintered hydroxyapatite–aluminum oxide–carbon nanotube composite. *Mater. Sci. Eng. C* **30**, 1162–1169 (2010).
38. Ogihara, N. et al. Biocompatibility and bone tissue compatibility of alumina ceramics reinforced with carbon nanotubes. *Nanomedicine (Lond)* **7**, 981–993 (2012).
39. Ormsby, R. et al. Fatigue and biocompatibility properties of a poly(methyl methacrylate) bone cement with multi-walled carbon nanotubes. *Acta Biomater.* **8**, 1201–1212 (2012).
40. Sato, Y. et al. Influence of length on cytotoxicity of multi-walled carbon nanotubes against human acute monocytic leukemia cell line THP-1 in vitro and subcutaneous tissue of rats in vivo. *Mol. Biosyst.* **1**, 176–182 (2005).
41. Samorì, C. et al. Potentiometric titration as a straightforward method to assess the number of functional groups on shortened carbon nanotubes. *Carbon* **48**, 2447–2454 (2010).
42. Light, W. G. & Wei, E. T. Surface charge and asbestos toxicity. *Nature* **265**, 537–539 (1977).
43. Fenoglio, I. et al. Structural defects play a major role in the acute lung toxicity of multiwall carbon nanotubes: Physicochemical aspects. *Free Radic. Biol. Med.* **40**, 1227–1233 (2006).
44. Matsuno, H., Yokoyama, A., Watari, F., Uo, M. & Kawasaki, T. Biocompatibility and osteogenesis of refractory metal implants, titanium, hafnium, niobium, tantalum and rhenium. *Biomaterials* **22**, 1253–1262 (2001).
45. Goodlick, L. A. & Kane, A. B. Role of reactive oxygen metabolites in crocidolite asbestos toxicity to mouse macrophages. *Cancer Res.* **46**, 5558–5566 (1986).
46. Karnovsky, M. L. & Badwey, J. A. Determinants of the production of active oxygen species by granulocytes and macrophages. *J. Cli. Chem. Clin. Biochem.* **21**, 545–553 (1983).
47. Ejiri, S. et al. An ultrastructural study on the multinucleation process of mouse alveolar macrophages induced by 1α,25-dihydroxyvitamin D$_3$. *J. Bone Miner. Res.* **2**, 547–557 (1987).
48. Poland, C. A. et al. Carbon nanotubes introduced into the abdominal cavity of mice show asbestos like pathogenicity in a pilot study. *Nat. Nanotech.* **3**, 423–428 (2008).
49. Nagai, H. et al. Diameter and rigidity of multiwalled carbon nanotubes are critical factors in mesothelial injury and carcinogenesis. *Proc. Natl. Acad. Sci. U. S. A.* **108**, E1330–E1338 (2011).
50. Bianco, A., Kostarelos, K. & Prato, M. Making carbon nanotubes biocompatible and biodegradable. *Chem. Comm.* **47**, 10182–10188 (2011).
51. Liu, Y., Zhao, Y., Sun, B. & Chen, C. Understanding the toxicity of carbon nanotubes. *Acc. Chem. Res.* **46**, 702–713 (2013).
52. Al-Jamal, K. T. et al. Degree of chemical functionalization of carbon nanotubes determines tissue distribution and excretion profile. *Angew. Chem. Int. Ed.* **51**, 6389–6393 (2012).
53. Delogu, L. G. et al. Ex vivo impact of functionalized carbon nanotubes on human immune cells. *Nanomedicine (Lond)* **7**, 231–243 (2012).
54. Ali-Boucetta, H. et al. Asbestos-like pathogenicity of long carbon nanotubes alleviated by chemical functionalization. *Angew. Chem. Int. Ed.* **52**, 2274–2278 (2013).
55. Lenihan, J. S., Gavalas, V. G., Wang, J. Q., Andrews, R. & Bachas, L. G. Protein immobilization on carbon nanotubes through a molecular adapter. *J. Nanosci. Nanotechnol.* **4**, 600–604 (2004).
56. Speck, J. S., Endo, M. & Dresselhaus, M. S. Structure and intercalation of thin benzene derived carbon fibers. *J. Cryst. Growth* **94**, 834–848 (1989).
57. Endo, M. et al. Pyrolytic carbon nanotubes from vapor-grown carbon fibers. *Carbon* **33**, 873–881 (2005).
58. Sakaguchi, N., Watari, F., Yokoyama, A. & Nodasaka, Y. High-resolution electron microscopy of multi-wall carbon nanotubes in the subcutaneous tissue of rats. *J. Electron Microsc.* **57**, 159–164 (2008).
59. Takanashi, S. et al. Carcinogenicity evaluation for the application of carbon nanotubes as biomaterials in rasH2 mice. *Sci. Rep.* **2**, 498–504 (2012).

Acknowledgements

Author contributions

Y.S. and A.Y. designed the study. Y.S., A.Y. and M.Y. analyzed the data and wrote the manuscript. Y.S., A.Y., Y.N., T.K., K.M., H.M, E.N., T.N., M.Z., M.Y., H.H., R.A., O.T., H.S. and T.K. performed the experiments. E.N., M.Y., H.H. and T.K. contributed to discussions. F.W. and K.T. supervised the project. All authors discussed the results and commented on the manuscript.

Additional information

Supplementary information accompanies this paper at http://www.nature.com/scientificreports

Competing financial interests: The authors declare no competing financial interests.